Research Article | Vol. 32, No. 26 / 16 Dec 2024 / Optics Express 45436

Optics EXPRESS

Diverse interlocked switching waves in cavity-enhanced second-harmonic generation

GANGZHOU WU,[1] CHONG HOU,[1] YATING WEI,[1] SHIHUA CHEN,[1,2,*] TONG LIN,[3,4] FABIO BARONIO,[5,6] AND ZHENHUA NI[1,2,7]

[1]School of Physics and Frontiers Science Center for Mobile Information Communication and Security, Southeast University, Nanjing 211189, China
[2]Purple Mountain Laboratories, Nanjing 211111, China
[3]Advanced Photonics Center, School of Electronic Science and Engineering, Southeast University, Nanjing 210096, China
[4]State Key Laboratory of Silicon and Advanced Semiconductor Materials, Zhejiang University, Hangzhou 310027, China
[5]Department of Information Engineering, University of Brescia and INO CNR, Via Branze 38, 25123 Brescia, Italy
[6]fabio.baronio@unibs.it
[7]zhni@seu.edu.cn
[*]cshua@seu.edu.cn

Abstract: We investigate the intriguing dynamics and existence conditions of temporal two-color flat-top solitons, termed interlocked switching waves (ISWs), in driven quadratic microresonators via a phase-matched second-harmonic generation process. We show that the formation of two-color ISWs relies strongly upon the pump frequency detuning, the group-velocity dispersion, and the temporal walk-off, and that the ISWs at the negative detuning may behave differently from the ones formed at the positive detuning, due to the asymmetric modulation instability of homogeneous steady-state solutions. In contrast to previous predictions, stable ISW states are found to occur as well on interacting harmonics that both have anomalous group-velocity dispersions when prepared at the negative detuning. Moreover, we unveil that large temporal walk-off contributes to the formation of two-color ISWs at the positive detuning but tends to deteriorate at the negative detuning. Our results help improve our understanding of two-color ISWs and thereby pave the way for highly efficient octave-spanning dual-band comb generation.

1. Introduction

Over the past decade, particularly since its experimental realization first in a passive ring cavity [1] and later in an optical microresonator [2], temporal dissipative Kerr soliton (DKS) has attracted increasing attention, because of its fundamental scientific interest [3,4] and its potential to producing low-power, fully coherent, chip-scale broadband frequency combs [5,6]. Contrarily to the soliton states in integrable systems [7], DKSs in microresonators represent a self-reinforcing localized structure that results from the double balance between dispersion and nonlinearity as well as between cavity loss and parametric gain [1–3]. The temporal dynamics of DKSs and the associated Kerr comb generation can be well understood by coupled-mode equations involving a limited number of modes [8] or by the driven Lugiato-Lefever equation that considers a large number of modes [9,10]. Thanks to the double balance, the DKSs are inherently robust against external perturbations and can even recover themselves from complete disruption [4], behaving like a strange attractor in nonlinear chaotic systems [11]. This strong stability along with coherent broadband comb spectra enables such dissipative soliton states versatile in numerous applications, such as terabit coherent communications [12,13], ultrafast distance measurements [14], chip-scale optical clocks [15], and astrophysical spectrometer calibrations [16], to name a few.

#542276 https://doi.org/10.1364/OE.542276
Journal © 2024 Received 13 Sep 2024; revised 9 Nov 2024; accepted 11 Nov 2024; published 2 Dec 2024

Optics EXPRESS

Optical Kerr microcavities that offer small cavity-mode volume and high quality (Q) factor for light-matter interaction [17] are also a promising platform for studying other intriguing soliton dynamics, which include Turing rolls [2,6], dark pulses [18,19] (also referred to as switching waves [20–22]), flat-top solitons (sometimes called platicons) [23,24], soliton molecules [25], dark-bright soliton bound states [26], and even optical rogue waves [27] or chaotic modulation instability states [28]. Among those coherent optical pulse structures, the dark pulses, the switching waves, and the so-called platicons actually refer to the same objects, as they arise from the interlocking of two separate wave fronts that connect high and low stationary states. As a result, such localized structures are able to form in Kerr microresonator with normal group-velocity dispersion (GVD) only [22–24], in sharp contrast to the DKSs which generally require anomalous GVD. It has turned out that, from the perspective of generation condition and comb conversion efficiency, coherent locked front structures indeed outperform the DKSs [23,29–31], in spite of involving a narrower pump-resonance detuning range [24]. In this article, we would term them interlocked switching waves (ISWs) [20,22], for the convenience of discussion.

Although Kerr soliton microcombs have made extraordinary progress, it is desirable to exploit quadratic solitons [32,33] to create frequency combs in optical microresonators containing only $\chi^{(2)}$ nonlinearity, by means of the second-harmonic generation (SHG) process [34–37] or the optical parametric oscillation (OPO) process [38–41]. It has been demonstrated that these quadratic combs thus obtained possess a relatively low power threshold and high conversion efficiency, due to the relatively large $\chi^{(2)}$ susceptibility as compared to the third-order optical susceptibility [42] and a comparably high Q-factor that has been achieved for on-chip quadratic micro rings [43]. Particularly, the above cascaded SHG/OPO process inherently gives rise to dual-band comb spectra on its fundamental frequency (FF) and second-harmonic (SH) components that are suitable for on-chip implementation of $1f-2f$ comb self-referencing and octave-spanning comb generation [42,44]. Efforts were also made to achieve combined Kerr and quadratic combs, which have potential to cover the ultraviolet and mid-infrared regimes [45–47]. We should mention that, apart from the above investigations on temporal pulse dynamics, there have been extensive studies on spatial cavity soliton dynamics in driven quadratic cavities for a long time [48,49], which are very similar to their temporal counterparts because of the space-time duality between diffraction and GVD, though they have a different physical origin.

Recently, there is considerable and growing interest in exploring the specific temporal ISW dynamics in optical microresonators made from quadratic materials [50–53]. It has pointed out that such two-color ISWs are only possible for interacting harmonics that have opposite GVDs [50,51]. In this article, we revisit the complex dynamics of two-color ISWs formed in quadratic microring resonators, from a modulation instability (MI) perspective [54–56]. We show that the dynamics of two-color ISWs can be well explained with the baseband MI theory [57–59] and would behave differently at the positive and negative pump frequency detunings, due to the asymmetric MI induced at these laser-cavity detunings. In contrast to previous findings [50,51], our results reveal that the two-color ISWs are also available for same anomalous GVDs occurring at both FF and SH components, when prepared at negative pump detunings. We also demonstrate that the temporal walk-off [35,60] have a significant yet distinct impact on the formation of two-color ISWs at different pump detunings, using the conventional frequency scan method.

The subsequent sections are organized as follows. In Sec. 2, we present the coupled mean-field equations and discuss their steady-state and two-color ISW solutions. In Sec. 3, we perform an MI analysis of the stationary state solutions, which is closely related to the formation of ISWs. We then discuss in Secs. 4 and 5 the dynamics of two-color ISWs in the absence/presence of temporal walk-off, respectively. Finally, we conclude our results in Sec. 6.

Optics EXPRESS

2. Coupled wave equations and switching wave solutions

For our studies, we consider a phase-matched SHG process $\omega_0 + \omega_0 = 2\omega_0$ involving the FF field E_1 and the SH field E_2 in a dispersive quadratic ring resonator of circumference L that is driven by a continuous-wave (cw) field $E_{\rm in}$ at carrier frequency ω_0. The cavity is supposed to be resonant with both fields and have high-finesse around both FF (ω_0) and SH ($2\omega_0$) frequencies. For the sake of simplicity, we assume the spatial diffraction to be negligible and let the wave-vector mismatch between two cavity fields be vanishing, i.e., $\Delta k = 2k(\omega_0) - k(2\omega_0) \approx 0$. In this doubly resonant configuration and neglecting the higher-order nonlinear and dispersive effects, the above cavity-enhanced SHG can be governed by two coupled mean-field equations [35,36]:

$$it_R\frac{\partial E_1}{\partial \xi} = (\delta_1 - i\alpha_1)E_1 + \frac{Lk_1''}{2}\frac{\partial^2 E_1}{\partial T^2} - \chi L E_2 E_1^* + i\sqrt{\theta_1}E_{\rm in}, \tag{1}$$

$$it_R\frac{\partial E_2}{\partial \xi} = (\delta_2 - i\alpha_2)E_2 - i\Delta k' L\frac{\partial E_2}{\partial T} + \frac{Lk_2''}{2}\frac{\partial^2 E_2}{\partial T^2} - \chi L E_1^2, \tag{2}$$

where $E_{1,2}(\xi, T)$ are slowly varying field envelopes, with ξ being the "slow time" that is a multiple of the cavity round-trip time $t_R = \mathrm{FSR}^{-1}$ (FSR means free spectral range) and T the "fast time" that is measured in a reference frame comoving at the group velocity of the FF wave. Here, $\delta_{1,2}$ represent the phase detuning of the intracavity fields $E_{1,2}$ from their respective cavity resonance, $\alpha_{1,2}$ are half of the total cavity power losses per round trip for light at ω_0 and $2\omega_0$, $k''_{1,2} = d^2k/d\omega^2|_{\omega_0,2\omega_0}$ are the GVD coefficients for specific wavenumber $k(\omega)$, and $\Delta k' = dk/d\omega|_{2\omega_0} - dk/d\omega|_{\omega_0}$ denotes temporal walk-off arising from group-velocity mismatch. Besides, θ_1 represents the power transmission coefficient of the coupler through which the pump field $E_{\rm in}$ is injected into the cavity. The parameter $\chi = 2\sqrt{2}\omega_0\chi^{(2)}_{\rm eff}/\sqrt{c^3 n^2_{\omega_0} n_{2\omega_0}\epsilon_0}$ characterizes the nonlinearity of quadratic medium [35], where $\chi^{(2)}_{\rm eff}$ is an effective second-order susceptibility, $n_{\omega_0,2\omega_0}$ are the refractive indices measured at ω_0 and $2\omega_0$, c is the speed of light in vacuum, and ϵ_0 is the permittivity of free space.

Using the change of variables $t = \xi/\xi_0$, $\tau = T/T_0$, and $u_{1,2} = E_{1,2}/\sqrt{P}$, where $\xi_0 = t_R/\alpha_1$, $T_0 = \sqrt{Lk_1''/\alpha_1}$, and $P = \alpha_1^2/\chi^2 L^2$, one can transform Eqs. (1) and (2) into dimensionless coupled mean-field equations:

$$i\frac{\partial u_1}{\partial t} = (\Delta_1 - i)\,u_1 + \frac{\beta_2^{\rm FF}}{2}\frac{\partial^2 u_1}{\partial \tau^2} - u_1^* u_2 + iF, \tag{3}$$

$$i\frac{\partial u_2}{\partial t} = (\Delta_2 - i\alpha)\,u_2 - id\frac{\partial u_2}{\partial \tau} + \frac{\beta_2^{\rm SH}}{2}\frac{\partial^2 u_2}{\partial \tau^2} - u_1^2. \tag{4}$$

Now, the intracavity fields $u_{1,2}(t, \tau)$ have been normalized by the square root of power $\sqrt{P}$, and t is the "slow-time" variable on the scale of the cavity photon lifetime t_R/α_1, and τ is the "fast-time" variable in units of the pulse width T_0 . The other parameters in Eqs. (3) and (4) are defined by $\beta_2^{\rm FF} = k_1''/|k_1''| = \pm 1$, $\beta_2^{\rm SH} = k_2''/|k_1''|$, $d = \Delta k'\sqrt{L/\alpha_1|k_1''|}$, $\alpha = \alpha_2/\alpha_1$, $\Delta_{1,2} = \delta_{1,2}/\alpha_1$, and $F = \sqrt{\theta_1}\chi E_{\rm in} L/\alpha_1^2$, which stand for the anomalous ($\beta_2^{\rm FF} = -1$) or normal ($\beta_2^{\rm FF} = +1$) GVD of the FF wave, the relative GVD of the SH wave, the normalized temporal walk-off, the relative loss rate intended for the SH wave, the laser-cavity detunings, and the pump excitation intensity, respectively. When $F = 0$, Eqs. (3) and (4) can be reduced to the ones in Refs. [33,61,62], which are basic models governing the evolution of quadratic solitons in bulk quadratic crystals [32]. It should be noted that Eqs. (3) and (4) can also describe the interaction of two beams focused in one transverse dimension (e.g., in a Fabry-Perot cavity filled with a quadratic medium), when replacing τ by x and letting d be the spatial birefringence walk-off [63].

Optics EXPRESS

For our present purposes, we consider the driven dispersive microring resonators with $F \neq 0$ and assume that the losses experienced by the FF and SH fields are equal and the cavity detunings satisfy perfect phase matching, i.e., $\alpha = 1$ and $\Delta_2 = 2\Delta_1$ [36]. Under the circumstances, one can find that Eqs. (3) and (4) admit the homogeneous steady-state (HSS) solutions

$$u_1^h = \frac{F}{1 + i\Delta_1 + I_1/(i2\Delta_1 + 1)}, \quad u_2^h = \frac{(u_1^h)^2}{2\Delta_1 - i}, \tag{5}$$

where the steady-state intensity $I_1 = |u_1^h|^2$ of the FF field is determined by the cubic equation:

$$I_1[(I_1 - 2\Delta_1^2 + 1)^2 + 9\Delta_1^2] - F^2(4\Delta_1^2 + 1) = 0. \tag{6}$$

Actually, the three roots of Eq. (6) can be explicitly written as

$$I_1^t = \frac{K}{6} + \frac{2W}{3K} + \frac{4}{3}\Delta_1^2 - \frac{2}{3}, \tag{7}$$

$$I_1^b = -\frac{K}{6}e^{-i\pi/3} - \frac{2W}{3K}e^{i\pi/3} + \frac{4}{3}\Delta_1^2 - \frac{2}{3}, \tag{8}$$

$$I_1^m = -\frac{K}{6}e^{i\pi/3} - \frac{2W}{3K}e^{-i\pi/3} + \frac{4}{3}\Delta_1^2 - \frac{2}{3}, \tag{9}$$

where $W = 4\Delta_1^4 - 31\Delta_1^2 + 1$, $K = (4Q + 4\sqrt{\Delta})^{1/3}$, $Q = 27F^2(4\Delta_1^2 + 1) - 2(2\Delta_1^2 - 1)(4\Delta_1^4 + 77\Delta_1^2 + 1)$, and $\Delta = Q^2 - 4W^3$ is the discriminant of Eq. (6). Here I_1^t, I_1^b, and I_1^m, if positive, denote the high (or top), low (or bottom), and middle values of the HSS intensity of FF field, respectively. The SH field is dynamically slaved to the FF field, and thus once the $I_1^{t,b,m}$ is known, the HSS intensity of the SH field follows with $I_2^{t,b,m} = (I_1^{t,b,m})^2/(4\Delta_1^2 + 1)$.

As one can see, these HSS solutions (5) only involve two free parameters F and Δ_1, which offers great convenience for our subsequent discussions. Further, when the discriminant fulfils $\Delta \leqslant 0$, all the three roots $I_1^{t,b,m}$ of Eq. (6) are real and thus the HSS solutions (5) would exhibit bistability. Thus $\Delta = Q^2 - 4W^3 \leqslant 0$ defines the bistable domain. It is revealed that only the HSS solutions with high and low intensities ($I_{1,2}^{t,b}$) are stable, whereas the one with $I_{1,2}^m$ intensity is unstable. Figure 1(a) illustrates the evolution of the HSS intensities versus the detuning Δ_1 for given $F = 9.2$, where the unstable intensities are indicated by dash-dotted lines. Obviously, for $F = 9.2$, the minimum ($|\Delta_1^{\min}| \simeq 3.89$) and maximum ($|\Delta_1^{\max}| \simeq 4.49$) values of the detuning Δ_1 that admits bistable HSS solutions can be found by the marginal stability condition

$$Q^2 = 4W^3. \tag{10}$$

Likewise, using Eqs. (7)–(9), one can determine the evolution of the HSS intensities with F for given Δ_1. We demonstrate this evolution in Fig. 1(b) for $\Delta_1 = 4.2$, where a landmark S shape is exhibited. In this case, the two extrema, $F^{\min} \simeq 8.56$ and $F^{\max} \simeq 10.56$, of the pump F allowing the bistable solutions are still determined by Eq. (10).

In addition to the HSS solutions (5), Eqs. (3) and (4) can also admit many other localized coherent structures such as temporal dissipative solitons [35], Turing roll patterns [37], and temporal simultons [40]. Here, what we are primarily concerned with is a special kind of localized flat-top solitons formed in the bistable region defined by Eq. (10), as seen in Fig. 1(c) where $\Delta_1 = 4.2$ and $F = 9.2$ are used. It is clearly seen that these flat-top solitons on both FF and SH components are composed of two stable HSS states that take the I_j^t and I_j^b intensities, respectively, where $j = 1, 2$. Physically, they arise from the interlocking of two separate switching waves that connect high and low HSS states [20–24,64]. For this reason, we call them ISWs [21,22], notwithstanding some other terminologies such as platicons [23] and dark pulses [18]

Optics EXPRESS

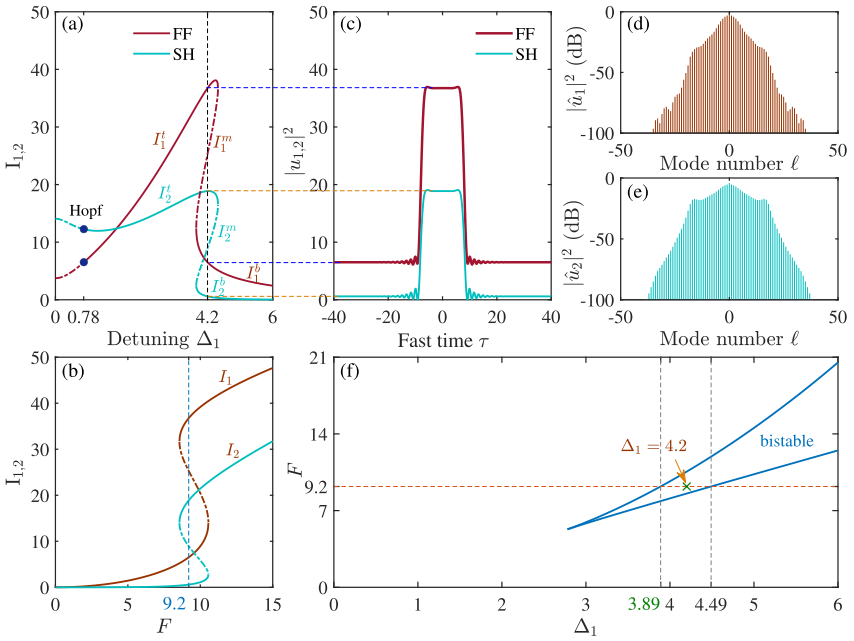

Fig. 1. Evolution of the high, low, and middle intensities of HSS solutions [Eqs. (7)–(9)] with respect to either of two free parameters, namely, (a) the pump frequency detuning Δ_1 for given $F = 9.2$, and (b) the pump intensity parameter F for given $\Delta_1 = 4.2$. In the bistable regime, while the middle intensities (dash-dotted curves) are entirely unstable, the high and low intensities (solid curves) are stable. (c) show the output profile of two-color ISWs at $t = 30$ calculating numerically from our dimensionless mean-field model, with the top intensity and background height being exactly determined by $I^t_{1,2}$ and $I^b_{1,2}$ in (a). The corresponding quadratic combs arising from such two-color ISWs are illustrated in (d) and (e). The system parameters used in (c)–(e) are given by $\Delta_1 = 4.2$, $F = 9.2$, $d = 0$, $\beta_2^{\rm FF} = -1$, and $\beta_2^{\rm SH} = 1$. The phase diagram in panel (f) gives the bistable regime inside which the two-color ISWs are able to form.

are also adopted in the literature. Actually, in a microring resonator, due to the periodicity, the pulse structure that looks dark in one part can be seen as being bright in the other part. Hence, in this work, we only investigate the temporal dynamics of flat-top ISW states shown in Fig. 1(c), but the results obtained can apply to their dark counterparts as well [18].

There are several typical features associated with such two-color ISWs. Specifically, in the temporal domain, the two-color ISWs possess an intensity-clamping property, which means their peak intensities depend only on F and Δ_1 and are tantamount to $I^t_{1,2}$, independently of the GVD and walk-off parameters appearing in the model. They may expand or shrink in width during propagation, depending mainly on the pump input F. At the Maxwell point, the ISWs preserve their shape as they propagate [65]. Similar behaviors also occur in spatially extended degenerate OPOs, where the two-dimensional domain walls with damped spatial oscillations can lock each other to form stable cavity solitons [66]. In the frequency domain, such flat-top temporal structures are generally endowed with an ultra-flat comb spectrum, particularly on the SH field component, as seen in Figs. 1(d) and 1(e), where $|\hat{u}_{1,2}|^2 = |\mathrm{FFT}(u_{1,2})|^2$ stand for the spectral intensities in units of decibel (dB). Though one often ascribed such a bat-wing comb feature to the cavity detuning [67,68], our preliminary numerical studies confirm that it results from the soliton Cherenkov radiation [69,70] mediated through GVD only, as was revealed in

Optics EXPRESS

Ref. [71]. Lastly, these two-color ISWs are only allowable within the bistable region surrounded by dark-blue curves in Fig. 1(f), which are determined by Eq. (10).

However, the intriguing properties of the two-color ISWs are far from being well understood. In the following, we will use the MI analysis to gain insight into the temporal and spectral dynamics of two-color ISWs, by taking into account the GVDs and temporal walk-off effects.

3. Modulation instability analysis

In nonlinear systems, MI is a fundamental property that leads to the growth of small perturbations on an unstable cw background and is closely related to the formation of solitons [54–59]. It is ubiquitous in nature, often called Bespalov-Talanov instability (in optics) or Benjamin-Feir instability (in hydrodynamics) [72]. In spatial dimension, MI can transform weakly modulated plane waves into spatially periodic patterns, as discussed in Refs. [73,74]. In frequency domain, the MI enables energy transfer between a strong single spectral component and sidebands [39,53,75]. Thus the MI analysis is extremely essential to an insight of the complicated dynamics of nonlinear, in particular, nonintegrable, systems [56,59].

For our current system, to find MI, let us suppose the HSS solutions are perturbed by

$$u_j = u_j^h + r_j \exp(\kappa t + i\Omega\tau) + w_j^* \exp(\kappa^* t - i\Omega\tau), \tag{11}$$

where u_j^h ($j = 1, 2$) are given by Eq. (5), $\Omega \in \mathbb{R}$ is the modulation frequency, and κ is the complex gain factor, and r_j and w_j denote the small amplitudes of complex Fourier modes [54]. Then, substituting Eq. (11) into Eqs. (3) and (4) followed by linearization, one can obtain a system of coupled linear equations about r_j and w_j. This system has a nontrivial solution only when κ and Ω satisfy the following dispersion relation:

$$(\kappa + \kappa_0)^4 + p\,(\kappa + \kappa_0)^2 + q\,(\kappa + \kappa_0) + r = 0, \tag{12}$$

where $\kappa_0 = id\Omega/2 + 1$ and

$$p = \frac{d^2\Omega^2}{2} + \Lambda_1^2 + \Lambda_2^2 + 4I_1 - I_2, \tag{13}$$

$$q = id\Omega(\Lambda_1^2 - \Lambda_2^2 - I_2), \tag{14}$$

$$r = \frac{d^4\Omega^4}{16} - \frac{d^2\Omega^2}{4}(\Lambda_1^2 + \Lambda_2^2 - 4I_1 - I_2) + (2I_1 - \Lambda_1\Lambda_2)^2 - I_2\Lambda_2^2, \tag{15}$$

$$\Lambda_1 = \frac{1}{2}\Omega^2\beta_2^{\mathrm{FF}} - \Delta_1, \quad \Lambda_2 = \frac{1}{2}\Omega^2\beta_2^{\mathrm{SH}} - 2\Delta_1. \tag{16}$$

Here I_1 and $I_2 = I_1^2/(4\Delta_1^2 + 1)$ are the intensities of the HSS solutions $u_{1,2}^h$ and thus are determined by Eqs. (7), (8) or (9).

In the case of no walk-off, i.e., when $d = 0$, the significant two roots of Eq. (12) can be simply expressed by radicals,

$$\kappa = \frac{1}{2}\sqrt{-2S \pm 2\sqrt{M^2 + 8I_1N}} - 1, \tag{17}$$

where $S = \Lambda_1^2 + \Lambda_2^2 + 4I_1 - I_2$, $M = -\Lambda_1^2 + \Lambda_2^2 + I_2$, and $N = (\Lambda_1 + \Lambda_2)^2 - I_2$. Noting that the other two roots of Eq. (12) have been disregarded, as they do not produce any valid results at all for our present purposes.

Optics EXPRESS

In the nonvanishing walk-off case ($d \neq 0$), one can exactly express the four roots of Eq. (12) as

$$\kappa_{1,2} = -R \pm \frac{1}{2}\sqrt{-4R^2 - 2p + \frac{q}{R}} - \kappa_0, \tag{18}$$

$$\kappa_{3,4} = R \pm \frac{1}{2}\sqrt{-4R^2 - 2p - \frac{q}{R}} - \kappa_0, \tag{19}$$

where

$$R = \frac{1}{2}\sqrt{-\frac{2p}{3} + \frac{1}{3}\left(A + \frac{\phi}{A}\right)}, \quad A = \left[\eta + \sqrt{\eta^2 - \phi^3}\right]^{1/3}, \tag{20}$$

with $\phi = p^2 + 12r$ and $\eta = p^3 - 36pr + 27q^2/2$.

Obviously, only when the real part of the roots κ of the quartic Eq. (12) is negative would the HSS solutions (5) be stable and therefore the localized ISWs exist. In other words, the ISW solutions do not exist in a regime where Re(κ)>0. The MI characteristics may become complicated when taking the dispersions and/or temporal walk-off into account. Here, to facilitate the MI analysis, we lift the positive-value constraints of $I_{1,2}^X$ ($X = t, b, m$) when substituting them into Eqs. (17)–(19). Then, we would call the MI caused by complex $I_{1,2}^X$ the virtual MI, to distinguish it from the genuine MI caused by positive $I_{1,2}^X$. With this methodology in mind, let us now inspect the intriguing ISW dynamics in detail according to two cases: the walk-off effect is absent ($d = 0$) and the walk-off is not vanishing ($d \neq 0$).

4. Two-color interlocked switching waves without walk-off

Based on Eq. (17), we find more interesting results about the two-color ISWs. Firstly, we show that the baseband MI determine exactly the existence region of the ISWs, provided that the Turing instability (TI) does not emerge. Here, we consider the TI to be a special kind of MI that satisfies Re(κ)>0 but Im(κ) = 0 [76], and refer to the baseband MI as one that allows the gain to exist even at infinitesimally small modulation frequencies $\Omega \to 0$ [57–59]. We demonstrate the map of MI gain denoted by Re(κ) with $I_{1,2} = I_{1,2}^t$ in Fig. 2(a) and the one with $I_{1,2} = I_{1,2}^b$ in Fig. 2(c), for given parameters $\beta_2^{\mathrm{FF}} = -1$ (anomalous GVD), $\beta_2^{\mathrm{SH}} = 1$ (normal GVD), $d = 0$ (no walk-off), $F = 9.2$, and $\Delta_1 = 4.2$. We do not show the MI map for $I_{1,2} = I_{1,2}^m$ here, as it has no bearing on the formation of ISWs. Noteworthily, here and in what follows, we have set in MI maps all negative gains that satisfy Re(κ)<0 to zero, in order to visualize better the existence domain of HSS solutions. It turns out that, as $\Omega \to 0$, the MI has a vanishingly small value at some Δ_1 positions indicated by white or green vertical dashed lines, which coincide exactly with the extrema of Δ_1 obtained from Eq. (10) [see Fig. 2(b)]. Clearly, it is seen from panel (a) that the HSS states with high intensity are stable between $0.78 < |\Delta_1| \leqslant |\Delta_1^{\max}| \simeq 4.49$, whereas the panel (c) suggests that the HSS states with low intensity are stable for $|\Delta_1| \geqslant |\Delta_1^{\min}| \simeq 3.89$. One can find that, for the current parameters used, no TI will appear in these MI maps. As a result, the localized flat-top ISWs composed of the stable high and low HSS states can exist in the whole bistable regime determined either by Eq. (10) or by the baseband MI theory [see the yellow shaped areas, i.e., $3.89 \leqslant |\Delta_1| \leqslant 4.49$, in Fig. 2(b)].

To confirm the above analytic predictions, we perform the numerical simulation of Eqs. (3) and (4) using the split-step Fourier method [77], under the same parameter condition except for letting Δ_1 vary from −6 to +6. Here, only the spectral results are provided with Figs. 2(d) and 2(e), clearly showing that the ISWs can exist in the region of $3.89 \leqslant |\Delta_1| \leqslant 4.49$, as predicted above. Our numerical simulations also show that, at $|\Delta_1| \leqslant 0.78$, there are emerging chaotic spectral structures, implying that no coherent soliton states are allowed in this region, as indicated in Fig. 2(b). This is caused by the onset of the Hopf instability which we denote by Re(κ)>0 but Im(κ) ≠ 0 (i.e., instability with complex eigenvalues) [78].

Optics EXPRESS

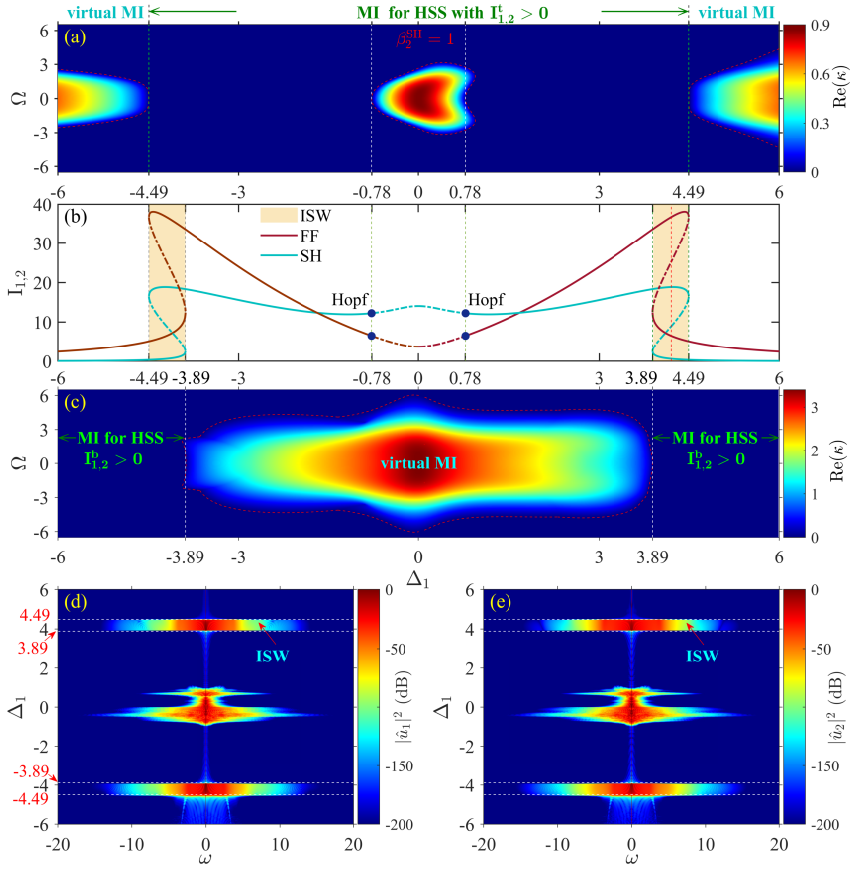

Fig. 2. MI maps Re(κ) versus (Δ_1, Ω) obtained from Eq. (17) for HSS solutions with: (a) high intensity $I^t_{1,2}$ and (c) low intensity $I^b_{1,2}$, where all negative gains are set to zero. The virtual MI refers to the one caused by complex $I^t_{1,2}$ (or $I^b_{1,2}$), wherein the HSS solutions with high (or low) intensity do not exist. The red dashed lines in (a) and (c) correspond to marginal stability curves Re(κ) = 0. (b) shows the evolution of three intensities of HSS solutions with Δ_1 for given $F = 9.2$, where the shaded bistable regimes are exactly consistent with existence regime of baseband MI. The black circles in (b) stand for the onset of Hopf instability. (d) and (e) show the numerical evolutions of output spectra $|\hat{u}_{1,2}|^2$ at $t = 30$ by seeding supercritical Gaussian pulses $u_{1,2}(t = 0, \tau) = I^t_{1,2} \exp(-\tau^2/64)$ into Eqs. (3) and (4) followed by sweeping the laser scan from $\Delta_1 = -6$ to $\Delta_1 = +6$ (forward frequency scan). The other system parameters are given by $F = 9.2$, $d = 0$, $\beta_2^{FF} = -1$, and $\beta_2^{SH} = 1$.

Secondly, we show that the MI map is asymmetric with respect to the pump frequency detuning Δ_1, and thus the ISWs excited by positive detuning can behave differently with those with negative detuning. Generally, keeping the FF GVD unvaryingly anomalous ($\beta_2^{FF} = -1$), the ISWs at positive detuning may disappear as the normal SH GVD decreases to a small value, as indicated by the yellow B(B′) and C(C′) crosses in Figs. 3(a) and 3(e). This is because a strong TI begins to emerge which eventually destroys the flat-top structure, resulting in the generation of multiple cavity-soliton states [1,79], as seen in Figs. 3(c), 3(d), 3(g), and 3(h). More specifically, the TI, which is initially absent at $\beta_2^{SH} = 1$ [see Fig. 2(a)], manifests itself now at $\beta_2^{SH} = 1/2$ [see those MI sidebands between green circles at $\Delta_1 = 4.0$ and green vertical dashed line at $\Delta_1 = 4.49$ in Fig. 3(a)] and hence inhibits ISWs to form in that interval of Δ_1. Generally, when the green

Optics EXPRESS

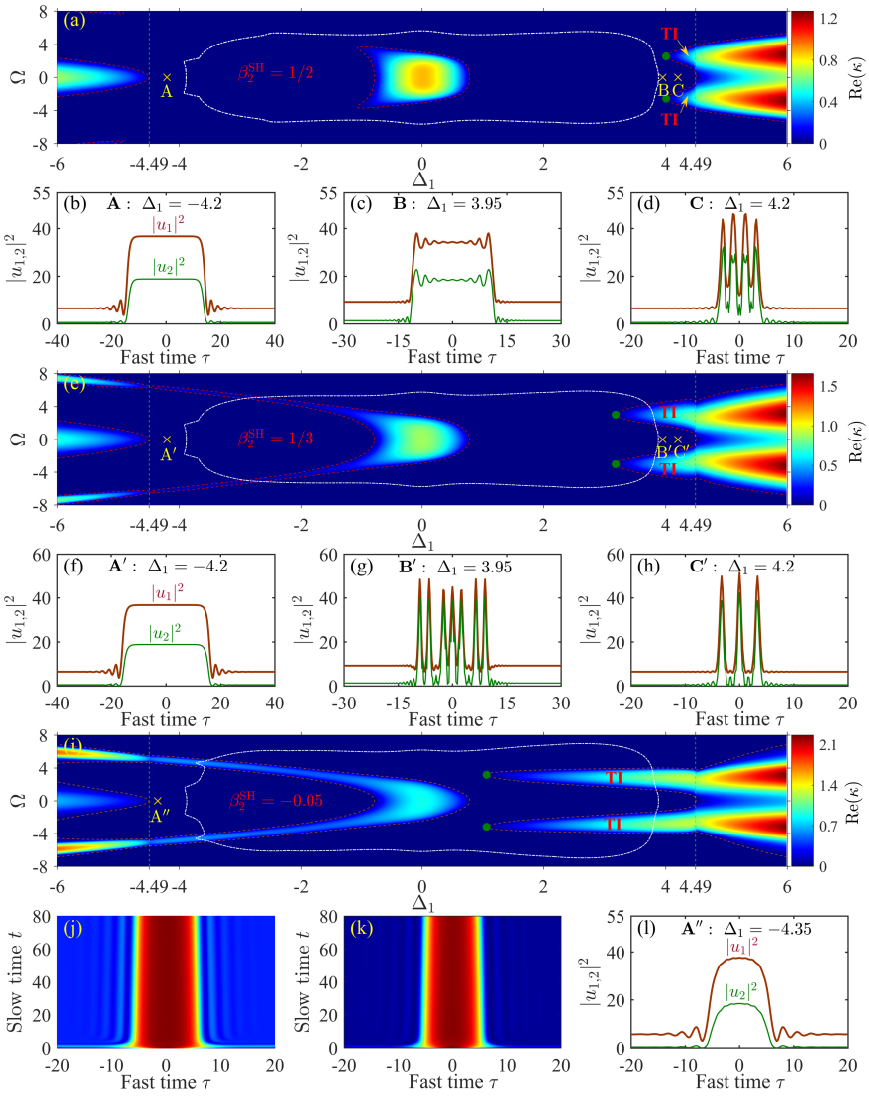

Fig. 3. Asymmetric MI maps versus Δ_1 for given $\beta_2^{FF} = -1$ (anomalous GVD), $F = 9.2$, $d = 0$, but with different β_2^{SH} values: (a) $\beta_2^{SH} = 1/2$ (normal GVD), (e) $\beta_2^{SH} = 1/3$ (normal GVD), and (i) $\beta_2^{SH} = -0.05$ (anomalous GVD). The white dotted curves in (a), (e), and (i) represent the marginal stability curves of the HSS solutions with low intensity. An MI branch between green circles and the green dashed line on the right is referred to as TI which satisfies Re(κ)>0 but Im(κ) = 0. (b), (c), and (d) show the temporal profiles of output pulses at $t = 80$, corresponding to the yellow crosses A ($\Delta_1 = -4.2$), B ($\Delta_1 = 3.95$), and C ($\Delta_1 = 4.2$) in (a), respectively. Similarly, the pulse profiles at the crosses A′, B′, and C′ in (e) are shown in (f), (g), and (h) and the pulse evolution for $\Delta_1 = -4.35$ at cross A″ in (i) has been indicated in (j) (the FF field), (k) (the SH field), and (l) (output profiles).

circles move leftward to a position where Δ_1<3.89, which corresponds to β_2^{SH}<0.47, ISW states are forbidden to form at positive detuning. However, for the negative detuning, the ISWs can still be well maintained, as seen in Figs. 3(b) and 3(f), corresponding to the yellow A(A′) crosses in the MI maps. Remarkably, we find that, even for an anomalous SH GVD ($\beta_2^{SH} = -0.05$ here), the

Optics EXPRESS

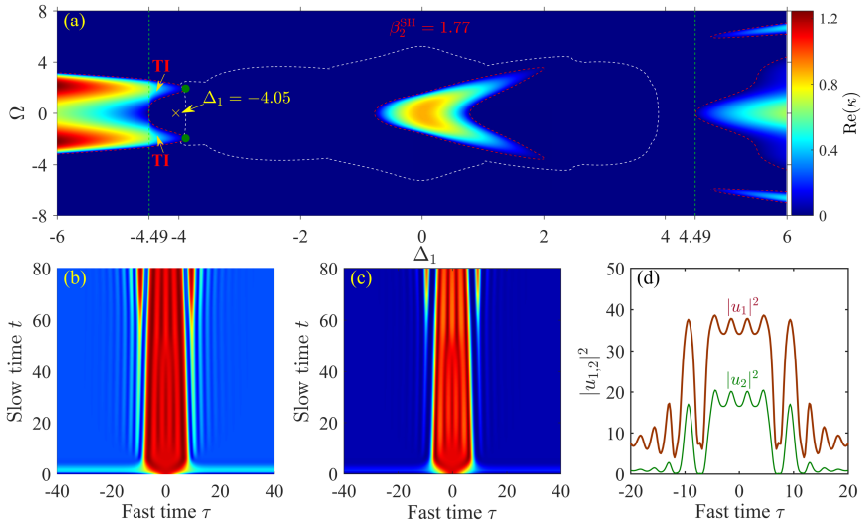

Fig. 4. (a) Asymmetric MI map versus (Δ_1, Ω) for $\beta_2^{SH} = 1.77$. (b), (c), and (d) show the pulse evolution at yellow cross ($\Delta_1 = -4.05$) in (a), under otherwise identical condition as in Fig. 3. The TI sidebands now manifest at the negative detuning side.

ISWs for $\Delta_1 = -4.35$ at cross A″ still possess a clear flat-top structure, as shown in Figs. 3(j)–3(l). This finding suggests the possibility that the two-color ISWs can exist for both anomalous GVDs experienced by FF and SH components, in sharp contrast to previous results where the two-color ISWs were reported only available for opposite GVDs [50–53].

Thirdly, we show that the main MI map in the plane (Δ_1, Ω) can flip as β_2^{SH} increases beyond 1, and thus the ISWs at negative detuning will disappear as well for large β_2^{SH}. We demonstrate in Fig. 4 the evolution of two-color ISWs occurring at $\Delta_1 = -4.05$ for $\beta_2^{SH} = 1.77$, with the other parameters being the same as used in Fig. 3. In this situation, the ISWs suffer from strong modulation soon after the input [see the simulation results in Figs. 4(b) and 4(c)], which show the temporal evolutions of the FF and SH fields, respectively, and their output profiles at $t = 80$ become broken [see Fig. 4(d)]. This is caused by the TI which now appears at the negative detuning side and inhibits the ISWs to form when $\beta_2^{SH} \geqslant 1.77$. However, in the positive detuning side, the two-color ISWs can still maintain a nice flat-top profile (not shown).

Lastly, we extensively simulate the coupled Eqs. (3) and (4) intended for the positive detuning ($\Delta_1 = 4.2$) and the negative detuning ($\Delta_1 = -4.2$), respectively, using the same Gaussian pulse input as used in Figs. 2(d) and 2(e). The numerical results are provided with Fig. 5, where, for simplicity, we keep $\beta_2^{FF} = -1$ fixed but let β_2^{SH} vary from −1 to 2. It is clear that in the positive detuning case, the localized dissipative structures manifest first as multiple soliton states or soliton molecules when $\beta_2^{SH}<0$ (anomalous GVD), accompanied by a broader multiple-FSR comb spectrum, but soon evolve into chaotical states when β_2^{SH} lies in small normal GVD regime, and eventually take the clean flat-top soliton states when $\beta_2^{SH} \geqslant 0.47$, as revealed by the temporal evolutions in Figs. 5(a) and 5(b) and the corresponding spectral evolutions in Figs. 5(c) and 5(d). By contrast, in the negative detuning case, the clean two-color ISW states can form within a broad range of β_2^{SH} ($-0.1<\beta_2^{SH}<1.77$ here), as indicated in Figs. 5(e)–5(h). Particularly, they can exist in the small normal, or weakly anomalous, GVD regime of β_2^{SH}, markedly different from that occurring in the positive detuning case.

We need to point out that the parameters used in our numerical simulations are accessible by realistic experimental conditions. To show this, let us consider a doubly resonant intracavity

Optics EXPRESS

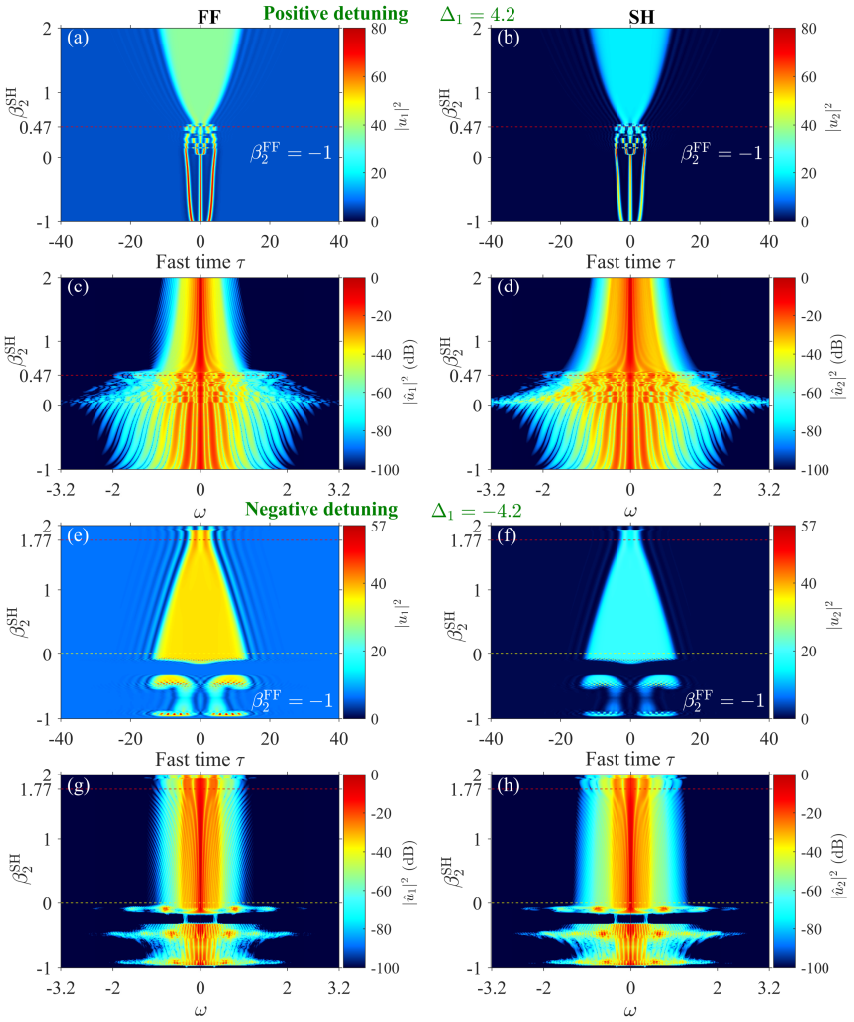

Fig. 5. (a,b) Temporal and (c,d) spectral evolutions of the output pulses with respect to the SH GVD parameter β_2^{SH} at the positive pump frequency detuning $\Delta_1 = 4.2$, for given $\beta_2^{FF} = -1$ (anomalous GVD), $F = 9.2$, and $d = 0$ (no walk-off). In a similar fashion, (e-h) show the temporal and spectral evolutions of output pulses at the negative detuning $\Delta_1 = -4.2$, with other parameters kept unchanged. The initial Gaussian pulse inputs seeded into the model are the same as in Fig. 2.

SHG system made of a 15 mm long periodically poled MgO-doped lithium niobate, as proposed in Ref. [36]. This configuration is experimentally feasible and was already used to observe the generation of optical frequency combs in 2015 [80]. The Sellmeier model and the related coefficients can be found in Ref. [81], from which one can calculate the refractive index $n(\lambda)$ and thus the GVD parameter $k''(\lambda) = \frac{d^2n(\lambda)}{d\lambda^2}\frac{\lambda^3}{2\pi c^2}$ at the specific wavelength $\lambda = 2\pi c/\omega$, as well as the required phase-matching conditions. For example, to realize an anomalous GVD at FF and a normal GVD at SH, as shown in Fig. 5, one can pump the system by a 2940 nm narrow-linewidth Er: YAG cw laser. In an *eeo* type I phase-matching situation, the dispersion coefficients at the FF ($\omega_0 = 2\pi \times 102\,\text{THz}$) and SH ($2\omega_0$) can read $k_1'' = -0.55\,\text{ps}^2/\text{m}$ and $k_2'' = 0.116\,\text{ps}^2/\text{m}$, corresponding to the normalized parameters $\beta_2^{FF} = -1$ and $\beta_2^{SH} = 0.21$, which

Optics EXPRESS

allow stable two-color ISWs at the negative pump detuning, as revealed in Figs. 5(e) and 5(f). Generally, the wave-number mismatch can be made nearly zero, i.e., $\Delta k = 2k_1 - k_2 - 2\pi/\Lambda \simeq 0$, using an appropriate poling period $\Lambda = 50\,\mu$m. If taking the typical nonlinear coefficient $\chi = 11.4\,\mathrm{W}^{-1/2}\mathrm{m}^{-1}$ and the cavity finesse $\pi/\alpha_1 = 160$ [36,80], the normalized pump parameter $F = 9.2$ used in our simulations corresponds to a driving power $P_{\mathrm{in}} \simeq 22\,$mW, which is also within the reach of commercial pump cw laser.

5. Interlocked switching waves with temporal walk off

Unlike its spatial counterpart which is usually weak for perfectly aligned pulsed beams, the temporal walk-off arises from the group-velocity mismatch $\Delta k'$ of two interacting pulses and can be made large even when the wave-vector mismatch Δk is vanishing [35,36,60]. Previous studies showed that large temporal walk-off effect can impact the soliton dynamics significantly,

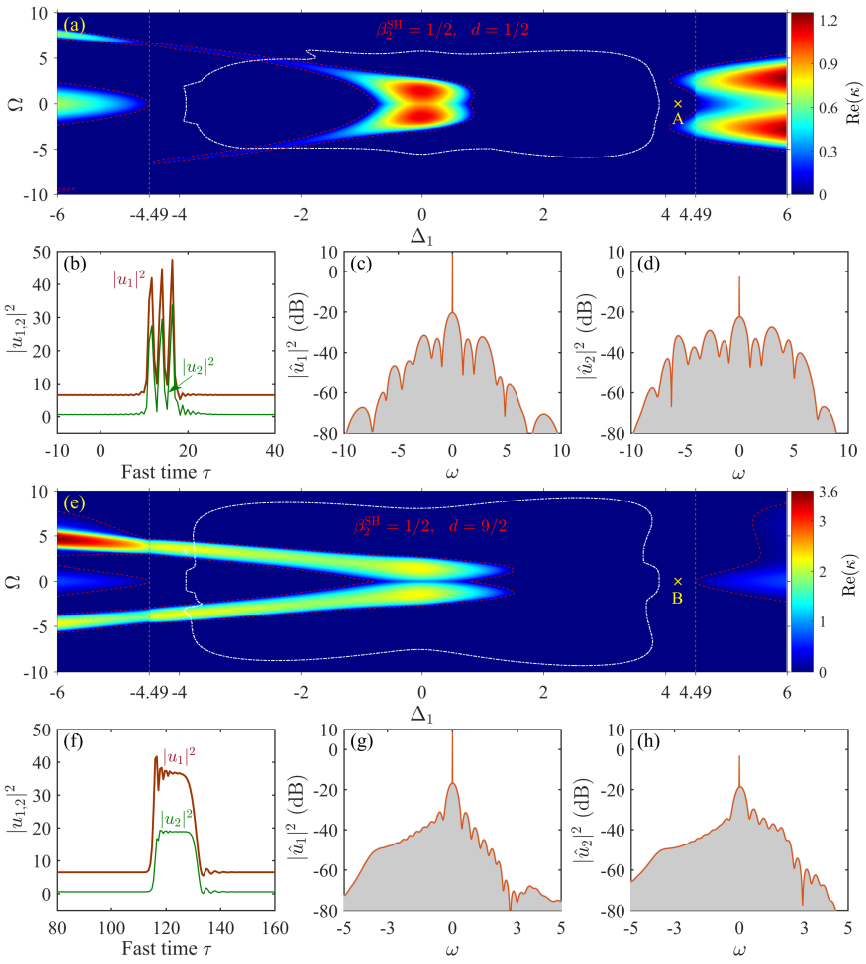

Fig. 6. Asymmetric MI map defined by Eqs. (18) and (19) versus (Δ_1, Ω) for $\beta_2^{\mathrm{FF}} = -1$ (anomalous), $\beta_2^{\mathrm{SH}} = 1/2$ (normal), and $F = 9.2$, but in the presence of temporal walk-off: (a) $d = 1/2$; (e) $d = 9/2$. The temporal profiles and the corresponding spectra of output pulses at $t = 80$ corresponding to the yellow cross A ($\Delta_1 = 4.2$) in (a) and B ($\Delta_1 = 4.2$) in (e) are illustrated in (b,c,d) and (f,g,h), respectively.

Optics EXPRESS

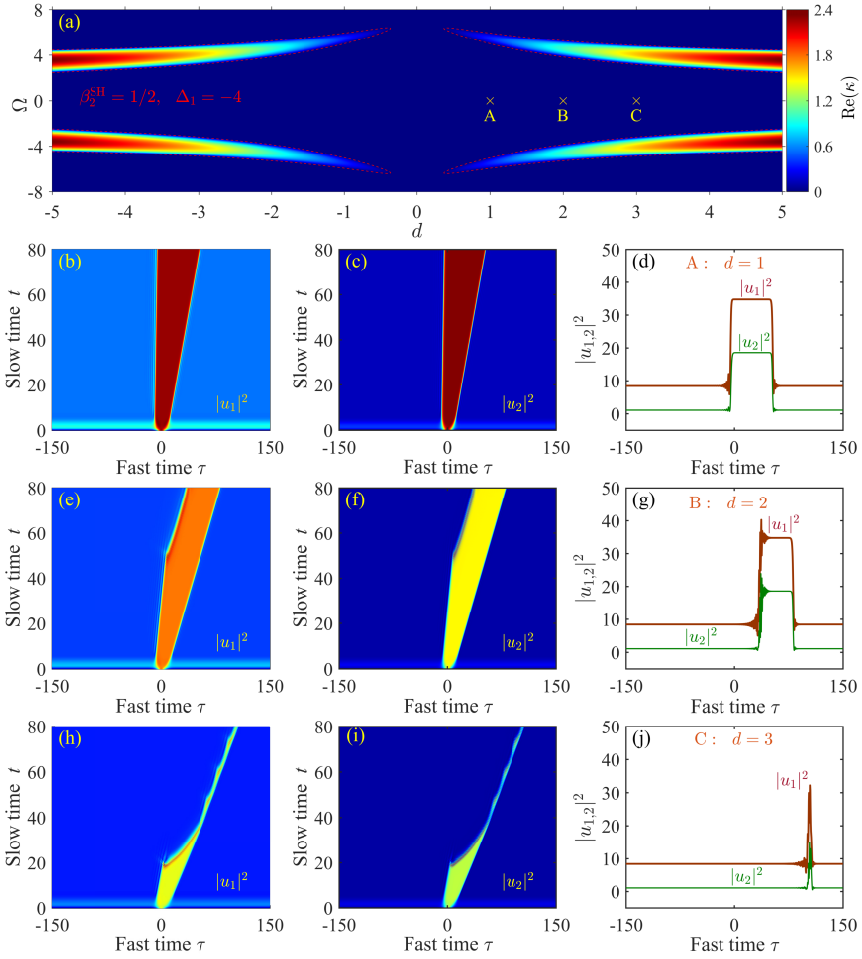

Fig. 7. MI map versus (d, Ω) for given $F = 9.2$, $\Delta_1 = -4$ (negative detuning), $\beta_2^{FF} = -1$ (anomalous GVD), and $\beta_2^{SH} = 1/2$ (normal GVD). The pulse evolutions corresponding to the yellow crosses A ($d = 1$), B ($d = 2$), and C ($d = 3$) in (a) are demonstrated in (b,c,d), (e,f,g), and (h,i,j), respectively, using the same Gaussian pulse input.

in both the normal and anomalous dispersion regimes [60,62]; For example, it can either stabilize the propagation of solitons in quadratic media [62] or trigger the formation of optical frequency combs in a singly resonant microcavity [35]. Here we show that the temporal walk-off can modify the MI map drastically, as implied by Eqs. (18) and (19). It not only enables the MI map to be asymmetric with respect to both Δ_1 and Ω, but also changes the MI characteristics associated to the formation of two-color ISWs.

For our comparative study, we consider the case in Fig. 3(a), in which the leftmost boundary of TI lies at $(\Delta_1^{TI}, \Omega) = (4, \pm 2.56)$ (see green circles therein) when the walk-off is absent. For that case, it has been shown that the ISWs will become breaking as $\Delta_1 > \Delta_1^{TI}$ [see Fig. 3(d)]. Now, we increase the walk-off parameter d from zero to a larger value, keeping the other parameters exactly the same as in Fig. 3(a). By means of Eqs. (18) and (19), we obtain numerically the MI maps shown in Fig. 6(a) and 6(e), which correspond to $d = 1/2$ and $d = 9/2$, respectively. It is seen that, due to the temporal walk-off, both MI maps become also asymmetric with respect to Ω (not only to Δ_1) and moreover some new MI structures emerge therein, as compared with

Optics EXPRESS

Fig. 3(a). Particularly, the MI domain corresponding to the original TI sideband becomes narrower and even disappears completely, as the parameter d grows. As a result, the two-color ISWs that suffer strong wave breaking at $d = 0$ tend to be redintegrated for a small $d = 1/2$ [see Fig. 6(b)] and eventually manifest for a large $d = 9/2$ [see Fig. 6(f)]. Of course, due to the temporal walk-off effect, both ISW components suffer a frequency shift in spectral evolution, and propagate in temporal domain with nonzero velocity. Meanwhile, at $d = 1/2$, the spectra display a multiple-FSR comb structure [see Figs. 6(c) and 6(d)], whereas at $d = 9/2$, the spectra feature a single-FSR comb, although asymmetric [see Figs. 6(g) and 6(h)]. This implies that for the positive detuning case, the temporal walk-off effect tends to stabilize, rather than deteriorate, the evolution of ISWs, akin to the case with travelling solitons in bulk quadratic media [61,62]. We note that, in spatially extended degenerate OPOs, the effect of spatial walk-off was also shown to contribute to the transverse pattern formation for positive signal detunings, by means of an order parameter description approach [82].

However, on the negative detuning side, the temporal walk-off will exert an opposite impact on the formation of two-color ISWs. In other words, it will disintegrate the pulses as the parameter d increases up to a large value. For illustration, we demonstrate in Fig. 7 the MI map in the plane (d, Ω) for given $F = 9.2$ and $\Delta_1 = -4$, and also three typical evolutions corresponding to A ($d = 1$), B ($d = 2$) and C ($d = 3$) points, respectively, keeping the other system parameters exactly the same as in Fig. 3(a). It is seen that at the A point in the MI map, the FF and SH ISWs are expanding during evolution [see Figs. 7(b)–7(d)], but tend to disintegrate (roughly after $t = 50$) at the B point [Figs. 7(e)–7(g)] and completely disappear at the C point because of strong Hopf instability [Figs. 7(h)–7(j)]. Obviously, this interesting property of the temporal walk-off can be used to tailor the shape of two-color ISWs.

6. Conclusion

In conclusion, we provided a systematic investigation of the dynamics and existence conditions of temporal two-color ISWs in driven dispersive quadratic microresonators, by means of a phase-matched SHG process, from the standpoint of MI. We revealed that the formation of two-color ISWs depends strongly on the pump frequency detunings, the GVDs, and the temporal walk-off, and can be well illuminated by the asymmetric MI of HSS solutions. It was found that such two-color ISWs would behave differently at the positive and negative pump detunings, since TI sidebands may emerge in either positive or negative detuning sides, but not in both. Particularly, our results clearly showed that, in contrast to previous predictions [50–53], stable ISW states are also available on interacting FF and SH components that both have anomalous GVDs when prepared at the negative detuning. In addition, the temporal walk-off was found to have a significant yet distinct impact on the ISW formation. Specifically, large temporal walk-off contributes to formation of two-color ISWs at the positive pump frequency detuning but tends to deteriorate it at the negative detuning. We anticipate that this work may help improve our understanding on two-color fat-top soliton states and thereby pave the way for high-efficient octave-spanning dual-band comb generation [42,47,83,84].

Funding. National Natural Science Foundation of China (12374301, 11974075, 62105061); National Key Research and Development Program of China (2021YFA1200700); State Key Laboratory of Silicon and Advanced Semiconductor Materials (SKL2023-04); Progetti di Ricerca di Interesse Nazionale (PRIN) (2020X4T57A); PRIN funded by European Union - Next Generation EU (20222NCTCY).

Disclosures. The authors declare no conflicts of interest.

Data availability. Data underlying the results presented in this paper are not publicly available at this time but may be obtained from the authors upon reasonable request.

References

1. F. Leo, S. Coen, P. Kockaert, *et al.*, "Temporal cavity solitons in one-dimensional Kerr media as bits in an all-optical buffer," Nat. Photonics **4**(7), 471–476 (2010).

Optics EXPRESS

2. T. Herr, V. Brasch, J. D. Jost, *et al.*, "Temporal solitons in optical microresonators," Nat. Photonics **8**(2), 145–152 (2014).
3. T. J. Kippenberg, A. L. Gaeta, M. Lipson, *et al.*, "Dissipative Kerr solitons in optical microresonators," Science **361**(6402), eaan8083 (2018).
4. M. Rowley, P.-H. Hanzard, A. Cutrona, *et al.*, "Self-emergence of robust solitons in a microcavity," Nature **608**(7922), 303–309 (2022).
5. M. A. Foster, J. S. Levy, O. Kuzucu, *et al.*, "Silicon-based monolithic optical frequency comb source," Opt. Express **19**(15), 14233–14239 (2011).
6. A. Pasquazi, M. Peccianti, L. Razzari, *et al.*, "Micro-combs: A novel generation of optical sources," Phys. Rep. **729**, 1–81 (2018).
7. Yu. S. Kivshar and G. P. Agrawal, *Optical Solitons: From Fibers to Photonic Crystals* (Academic, 2003), Chap. 1–4.
8. Y. K. Chembo and N. Yu, "Modal expansion approach to optical-frequency-comb generation with monolithic whispering-gallery-mode resonators," Phys. Rev. A **82**(3), 033801 (2010).
9. L. A. Lugiato and R. Lefever, "Spatial dissipative structures in passive optical systems," Phys. Rev. Lett. **58**(21), 2209–2211 (1987).
10. Y. K. Chembo and C. R. Menyuk, "Spatiotemporal Lugiato-Lefever formalism for Kerr-comb generation in whispering-gallery-mode resonators," Phys. Rev. A **87**(5), 053852 (2013).
11. J. He, P. Wang, R. He, *et al.*, "Elastic and inelastic collision dynamics between soliton molecules and a single soliton," Opt. Express **30**(9), 14218–14231 (2022).
12. P. Marin-Palomo, J. N. Kemal, M. Karpov, *et al.*, "Microresonator-based solitons for massively parallel coherent optical communications," Nature **546**(7657), 274–279 (2017).
13. B. Y. Kim, Y. Okawachi, J. K. Jang, *et al.*, "Turn-key, high-efficiency Kerr comb source," Opt. Lett. **44**(18), 4475–4478 (2019).
14. P. Trocha, M. Karpov, D. Ganin, *et al.*, "Ultrafast optical ranging using microresonator soliton frequency combs," Science **359**(6378), 887–891 (2018).
15. S. B. Papp, K. Beha, P. Del'Haye, *et al.*, "Microresonator frequency comb optical clock," Optica **1**(1), 10–14 (2014).
16. M.-G. Suh, X. Yi, Y.-H. Lai, *et al.*, "Searching for exoplanets using a microresonator astrocomb," Nat. Photonics **13**(1), 25–30 (2019).
17. K. J. Vahala, "Optical microcavities," Nature **424**(6950), 839–846 (2003).
18. X. Xue, Y. Xuan, Y. Liu, *et al.*, "Mode-locked dark pulse Kerr combs in normal-dispersion microresonators," Nat. Photonics **9**(9), 594–600 (2015).
19. P. Parra-Rivas, D. Gomila, E. Knobloch, *et al.*, "Origin and stability of dark pulse Kerr combs in normal dispersion resonators," Opt. Lett. **41**(11), 2402–2405 (2016).
20. S. Coen, M. Tlidi, Ph. Emplit, *et al.*, "Convection versus dispersion in optical bistability," Phys. Rev. Lett. **83**(12), 2328–2331 (1999).
21. E. Nazemosadat, A. Fülöp, Ó. B. Helgason, *et al.*, "Switching dynamics of dark-pulse Kerr frequency comb states in optical microresonators," Phys. Rev. A **103**(1), 013513 (2021).
22. M. H. Anderson, A. Tikan, A. Tusnin, *et al.*, "Dissipative solitons and switching waves in dispersion-modulated Kerr cavities," Phys. Rev. X **13**(1), 011040 (2023).
23. V. E. Lobanov, G. Lihachev, T. J. Kippenberg, *et al.*, "Frequency combs and platicons in optical microresonators with normal GVD," Opt. Express **23**(6), 7713–7721 (2015).
24. G. Lihachev, W. Weng, J. Liu, *et al.*, "Platicon microcomb generation using laser self-injection locking," Nat. Commun. **13**(1), 1771 (2022).
25. D. C. Cole, E. S. Lamb, P. Del'Haye, *et al.*, "Soliton crystals in Kerr resonators," Nat. Photonics **11**(10), 671–676 (2017).
26. S. Zhang, T. Bi, G. N. Ghalanos, *et al.*, "Dark-bright soliton bound states in a microresonator," Phys. Rev. Lett. **128**(3), 033901 (2022).
27. A. Coillet, J. Dudley, G. Genty, *et al.*, "Optical rogue waves in whispering-gallery-mode resonators," Phys. Rev. A **89**(1), 013835 (2014).
28. A. Lukashchuk, J. Liu, J. Riemensberger, *et al.*, "Chaotic microcomb-based parallel ranging," Nat. Photonics **17**(9), 814–821 (2023).
29. I. Rebolledo-Salgado, C. Quevedo-Galán, Ó. B. Helgason, *et al.*, "Platicon dynamics in photonic molecules," Commun. Phys. **6**(1), 303 (2023).
30. X. Xue, Y. Xuan, P.-H. Wang, *et al.*, "Normal-dispersion microcombs enabled by controllable mode interactions," Laser Photonics Rev. **9**(4), L23–L28 (2015).
31. V. E. Lobanov, N. M. Kondratiev, and I. A. Bilenko, "Thermally induced generation of platicons in optical microresonators," Opt. Lett. **46**(10), 2380–2383 (2021).
32. A. V. Buryak, P. Di Trapani, D. V. Skryabin, *et al.*, "Optical solitons due to quadratic nonlinearities: From basic physics to futuristic applications," Phys. Rep. **370**(2), 63–235 (2002).
33. C. R. Menyuk, R. Schiek, and L. Tornert, "Solitary waves due to $\chi^{(2)}$:$\chi^{(2)}$ cascading," J. Opt. Soc. Am. B **11**(12), 2434–2443 (1994).
34. J. U. Fürst, D. V. Strekalov, D. Elser, *et al.*, "Naturally phase-matched second-harmonic generation in a whispering-gallery-mode resonator," Phys. Rev. Lett. **104**(15), 153901 (2010).

Optics EXPRESS

35. F. Leo, T. Hansson, I. Ricciardi, *et al.*, "Walk-off-induced modulation instability, temporal pattern formation, and frequency comb generation in cavity-enhanced second-harmonic generation," Phys. Rev. Lett. **116**(3), 033901 (2016).
36. F. Leo, T. Hansson, I. Ricciardi, *et al.*, "Frequency-comb formation in doubly resonant second-harmonic generation," Phys. Rev. A **93**(4), 043831 (2016).
37. J. Szabados, D. N. Puzyrev, Y. Minet, *et al.*, "Frequency comb generation via cascaded second-order nonlinearities in microresonators," Phys. Rev. Lett. **124**(20), 203902 (2020).
38. V. Ulvila, C. R. Phillips, L. Halonen, *et al.*, "High-power mid-infrared frequency comb from a continuous-wave-pumped bulk optical parametric oscillator," Opt. Express **22**(9), 10535–10543 (2014).
39. S. Mosca, M. Parisi, I. Ricciardi, *et al.*, "Modulation instability induced frequency comb generation in a continuously pumped optical parametric oscillator," Phys. Rev. Lett. **121**(9), 093903 (2018).
40. M. Jankowski, A. Marandi, C. R. Phillips, *et al.*, "Temporal simultons in optical parametric oscillators," Phys. Rev. Lett. **120**(5), 053904 (2018).
41. I. Hendry, L. S. Trainor, Y. Xu, *et al.*, "Experimental observation of internally pumped parametric oscillation and quadratic comb generation in a $\chi^{(2)}$ whispering-gallery-mode microresonator," Opt. Lett. **45**(5), 1204–1207 (2020).
42. A. W. Bruch, X. Liu, Z. Gong, *et al.*, "Pockels soliton microcomb," Nat. Photonics **15**(1), 21–27 (2021).
43. R. Wolf, I. Breunig, H. Zappe, *et al.*, "Cascaded second-order optical nonlinearities in on-chip micro rings," Opt. Express **25**(24), 29927–29933 (2017).
44. P. Parra-Rivas, C. M. Arabí, and F. Leo, "Dissipative localized states and breathers in phase-mismatched singly resonant optical parametric oscillators: Bifurcation structure and stability," Phys. Rev. Res. **4**(1), 013044 (2022).
45. S. Miller, K. Luke, Y. Okawachi, *et al.*, "On-chip frequency comb generation at visible wavelengths via simultaneous second- and third-order optical nonlinearities," Opt. Express **22**(22), 26517–26525 (2014).
46. J. Hu, E. Nitiss, J. He, *et al.*, "Photo-induced cascaded harmonic and comb generation in silicon nitride microresonators," Sci. Adv. **8**(50), eadd8252 (2022).
47. G. Lin and Q. Song, "Kerr frequency comb interaction with Raman, Brillouin, and second order nonlinear effects," Laser Photonics Rev. **16**(1), 2100184 (2022).
48. C. Etrich, U. Peschel, and F. Lederer, "Solitary waves in quadratically nonlinear resonators," Phys. Rev. Lett. **79**(13), 2454–2457 (1997).
49. S. Longhi, "Spatial solitary waves and patterns in type II second-harmonic generation," Opt. Lett. **23**(5), 346–348 (1998).
50. V. E. Lobanov, N. M. Kondratiev, A. E. Shitikov, *et al.*, "Two-color flat-top solitonic pulses in $\chi^{(2)}$ optical microresonators via second-harmonic generation," Phys. Rev. A **101**(1), 013831 (2020).
51. V. E. Lobanov, "Two-color flat-top solitons in microresonator-based optical parametric oscillators," Phys. Rev. A **102**(1), 013518 (2020).
52. C. M. Arabí, P. Parra-Rivas, T. Hansson, *et al.*, "Localized structures formed through domain wall locking in cavity-enhanced second-harmonic generation," Opt. Lett. **45**(20), 5856–5859 (2020).
53. P. Parra-Rivas, C. M. Arabí, and F. Leo, "Dark quadratic localized states and collapsed snaking in doubly resonant dispersive cavity-enhanced second-harmonic generation," Phys. Rev. A **104**(6), 063502 (2021).
54. S. Trillo and M. Haelterman, "Pulse-train generation through modulational instability in intracavity second-harmonic generation," Opt. Lett. **21**(15), 1114–1116 (1996).
55. C. Pan, L. Bu, S. Chen, *et al.*, "Omnipresent coexistence of rogue waves in a nonlinear two-wave interference system and its explanation by modulation instability," Phys. Rev. Res. **3**(3), 033152 (2021).
56. S. Chen, L. Bu, C. Pan, *et al.*, "Modulation instability–rogue wave correspondence hidden in integrable systems," Commun. Phys. **5**(1), 297 (2022).
57. F. Baronio, M. Conforti, A. Degasperis, *et al.*, "Vector rogue waves and baseband modulation instability in the defocusing regime," Phys. Rev. Lett. **113**(3), 034101 (2014).
58. F. Baronio, S. Chen, Ph. Grelu, *et al.*, "Baseband modulation instability as the origin of rogue waves," Phys. Rev. A **91**(3), 033804 (2015).
59. S. Chen, F. Baronio, J. M. Soto-Crespo, *et al.*, "Versatile rogue waves in scalar, vector, and multidimensional nonlinear systems," J. Phys. A **50**(46), 463001 (2017).
60. A. Roy, R. Nehra, S. Jahani, *et al.*, "Temporal walk-off induced dissipative quadratic solitons," Nat. Photonics **16**(2), 162–168 (2022).
61. L. Bu, S. Chen, F. Baronio, *et al.*, "Resonant radiation emitted by solitary waves via cascading in quadratic media," Opt. Express **31**(5), 8307–8324 (2023).
62. L. Bu, G. Wu, C. Hou, *et al.*, "Soliton resonant radiation in phase-matched second-harmonic generation," Phys. Rev. A **109**(1), 013510 (2024).
63. M. Santagiustina, P. Colet, M. San Miguel, *et al.*, "Noise-sustained convective structures in nonlinear optics," Phys. Rev. Lett. **79**(19), 3633–3636 (1997).
64. N. N. Rozanov, V. E. Semenov, and G. Khodova, "Transverse structure of a field in nonlinear bistable interferometers. I. Switching waves and steady-state profiles," Sov. J. Quantum Electron. **12**(2), 193–197 (1982).
65. C. Fernandez-Oto, M. G. Clerc, D. Escaff, *et al.*, "Strong nonlocal coupling stabilizes localized structures: An analysis based on front dynamics," Phys. Rev. Lett. **110**(17), 174101 (2013).
66. G.-L. Oppo, A. J. Scroggie, and W. J. Firth, "From domain walls to localized structures in degenerate optical parametric oscillators," J. Opt. B: Quantum Semiclass. Opt. **1**(1), 133–138 (1999).

Optics EXPRESS

67. S. Malaguti, G. Bellanca, and S. Trillo, "Dispersive wave-breaking in coherently driven passive cavities," Opt. Lett. **39**(8), 2475–2478 (2014).
68. Y. Xu, A. Sharples, J. Fatome, *et al.*, "Frequency comb generation in a pulse-pumped normal dispersion Kerr mini-resonator," Opt. Lett. **46**(3), 512–515 (2021).
69. N. Akhmediev and M. Karlsson, "Cherenkov radiation emitted by solitons in optical fibers," Phys. Rev. A **51**(3), 2602–2607 (1995).
70. V. Brasch, M. Geiselmann, T. Herr, *et al.*, "Photonic chip-based optical frequency comb using soliton Cherenkov radiation," Science **351**(6271), 357–360 (2016).
71. L. Bu, F. Baronio, S. Chen, *et al.*, "Quadratic Peregrine solitons resonantly radiating without higher-order dispersion," Opt. Lett. **47**(10), 2370–2373 (2022).
72. G. Vanderhaegen, C. Naveau, P. Szriftgiser, *et al.*, "Extraordinary modulation instability in optics and hydrodynamics," Proc. Natl. Acad. Sci. USA **118**(14), e2019348118 (2021).
73. P. Lodahl and M. Saffman, "Pattern formation in singly resonant second-harmonic generation with competing parametric oscillation," Phys. Rev. A **60**(4), 3251–3261 (1999).
74. P. Lodahl, M. Bache, and M. Saffman, "Modification of pattern formation in doubly resonant second-harmonic generation by competing parametric oscillation," Opt. Lett. **25**(9), 654–656 (2000).
75. P. Ferro and S. Trillo, "Periodical waves, domain walls, and modulational instability in dispersive quadratic nonlinear media," Phys. Rev. E **51**(5), 4994–4998 (1995).
76. F. Copie, M. Conforti, A. Kudlinski, *et al.*, "Competing Turing and Faraday instabilities in longitudinally modulated passive resonators," Phys. Rev. Lett. **116**(14), 143901 (2016).
77. S. Chen, C. Pan, P. Grelu, *et al.*, "Fundamental Peregrine solitons of ultrastrong amplitude enhancement through self-steepening in vector nonlinear systems," Phys. Rev. Lett. **124**(11), 113901 (2020).
78. C. Milián and D. V. Skryabin, "Soliton families and resonant radiation in a micro-ring resonator near zero group-velocity dispersion," Opt. Express **22**(3), 3732–3739 (2014).
79. F. Leo, L. Gelens, P. Emplit, *et al.*, "Dynamics of one-dimensional Kerr cavity solitons," Opt. Express **21**(7), 9180–9191 (2013).
80. I. Ricciardi, S. Mosca, M. Parisi, *et al.*, "Frequency comb generation in quadratic nonlinear media," Phys. Rev. A **91**(6), 063839 (2015).
81. D. E. Zelmon, D. L. Small, and D. Jundt, "Infrared corrected Sellmeier coefficients for congruently grown lithium niobate and 5 mol. % magnesium oxide-doped lithium niobate," J. Opt. Soc. Am. B **14**(12), 3319–3322 (1997).
82. M. Santagiustina, P. Colet, M. S. Miguel, *et al.*, "Walk-off and pattern selection in optical parametric oscillators," Opt. Lett. **23**(15), 1167–1169 (1998).
83. I. Coddington, N. Newbury, and W. Swann, "Dual-comb spectroscopy," Optica **3**(4), 414–426 (2016).
84. Q. Wang, Z. Wang, H. Zhang, *et al.*, "Dual-comb photothermal spectroscopy," Nat. Commun. **13**(1), 2181 (2022).